Rapid Biomarker Screening of Alzheimer's Disease by Machine Learning and Graphene-Assisted Raman Spectroscopy

Ziyang Wang, Jiarong Ye, Li Ding, Tomotaroh Granzier-Nakajima, Shubhang Sharma, Isabelle Biase, Mauricio Terrones, Se Hoon Choi, Chongzhao Ran, Rudolph E. Tanzi, Sharon X. Huang, Can Zhang*, Shengxi Huang**

Z. Wang, L. Ding, Prof. S. Huang
Department of Electrical Engineering, The Pennsylvania State University, University Park, 16802, USA
E-mail: sjh5899@psu.edu

J. Ye, Prof. S. X. Huang
College of Information Sciences and Technology, The Pennsylvania State University, University Park, 16802, USA
E-mail: suh972@psu.edu

T. G-Nakajima, Prof. M. Terrones
Department of Physics, The Pennsylvania State University, University Park, 16802, USA

S. Sharma, I. Biase
Department of Computer Science, The Pennsylvania State University, University Park, 16802, USA

S. H. Choi, R. E. Tanzi, Prof. C. Zhang
Genetics and Aging Research Unit, McCance Center for Brain Health, MassGeneral Institute for Neurodegenerative Disease Department of Neurology, Massachusetts General Hospital, Harvard Medical School, 114 16th Street, Charlestown, MA, 02129, USA
E-mail: zhang.can@mgh.harvard.edu

Prof. C. Ran
Martinos Center for Biomedical Imaging, Massachusetts General Hospital, Harvard Medical school, 13th Street, Building149, Charlestown, MA, 02129, USA

Abstract

As the most common cause of dementia, Alzheimer's disease (AD) faces challenges in terms of understanding of pathogenesis, developing early diagnosis and developing effective treatment. Rapid and accurate identification of AD biomarkers in the brain will be critical to provide novel insights of AD. To this end, in the current work, we developed a system that can enable a rapid screening of AD biomarkers by employing Raman spectroscopy and machine learning analyses in AD transgenic animal brains. Specifically, we collected Raman spectra on slices of mouse brains with and without AD, and used machine learning to classify AD and non-AD spectra. By contacting monolayer graphene with the brain slices, we achieved significantly increased accuracy from 77% to 98% in machine learning classification. Further, we identified the Raman signature bands that are most important in classifying AD and non-AD samples. Based on these, we managed to identify AD-related biomolecules, which have been confirmed by biochemical studies. Our Raman-machine learning integrated method is promising to greatly accelerate the study of AD and can be potentially extended to human samples and various other diseases.

1. Introduction

Alzheimer's disease (AD), a progressive disorder of brain that damages memory and other brain functions, is the most common cause of dementia[1]. In 2015, about 29.8 million people worldwide were diagnosed with AD[2]. In recent years, a large number of research projects have been conducted to investigate the causes of AD regarding specific biomarkers. Olsson et al.[3] reviewed the literature and summarized that three core biomarkers, T-tau, P-tau and $A\beta_{42}$ are strongly associated with AD. Studies on essential AD biomarkers also led to a new era of treatment against cognitive impairment and AD[4,5]. However, the methods to investigate biomarkers including magnetic resonance imaging (MRI) and positron emission tomography (PET) are costly and time consuming[6,7]. In recent years, detection of disease biomarkers via immunoassay and fluorescence spectroscopy on blood and cerebrospinal fluid (CSF), has been intensively investigated in both preclinical and clinical stages[8–11], but they are limited in speed and multiplexity. Although the detection of disease biomarkers has significantly contributed to the decoding of the complex pathology of AD, numerous mysteries still exist around the causes of the disease and the failure of AD drug development[12]. To further decipher these mysteries, new methods to rapidly screen AD biomarkers from a huge number of candidate molecules are urgently needed.

Raman spectroscopy is a non-destructive and label-free molecular sensing method. By exciting the samples with a monochromatic laser and collecting the inelastically scattered signal from the analyte, a Raman spectrum is obtained, which provides the fingerprints of the analyte. Raman spectroscopy is potentially a high multiplexity and high specificity sensing technique due to the multiple and extremely narrow (typical full width at half maximum < 1 meV) Raman peaks in the spectra. Raman spectroscopy has been used to characterize a broad range of materials including semiconductors, nanomaterials, polymers, and biological samples[13]. In the biosensing domain, Raman spectroscopy has been demonstrated as being effective in detecting proteins, cells, viruses, biomarkers of various diseases etc., when combined with judiciously designed signal enhancement techniques, molecular conjugation methods, and signal reporting molecules[14–16]. In-vivo Raman sensing has also been exploited successfully to detect cancers and brain tumors, and to assist photothermal therapy and drug delivery[17].

Since Raman spectroscopy provides a desirable approach that meets clinical practice requirements with noninvasiveness and rapid diagnosis, it has been utilized in analyzing AD in blood plasma[18], investigating AD in brain hippocampus regions[6], imaging amyloid plaques in brain tissues[19], etc. The analyses of raw Raman spectra in previous works consist of spectral comparisons and principal component analysis (PCA)[20]. However, molecule identification by spectral comparison or PCA is unreliable when the intra-class spectral variability is too high, making the distinguishable patterns obscure[20]. In addition, spectral comparisons are limited on spotting visible patterns while neglecting distinguishable nuances that machine learning models can easily pick up.

In recent years, machine learning is thriving in fields of Raman spectroscopy analysis on biomedical applications such as cancer diagnosis[21], bacterial and viral infections[22], blood disorders and diabetes[23], kidney, heart, and thyroid diseases[24], autoimmune and neurodegenerative diseases[25]. Some commonly used machine learning models include support vector machine (SVM)[26], random forest classifier[27] and neural networks[28]. Besides achieving outstanding performance in classification, machine learning can interpret the correlation between Raman spectral ranges and diseases by providing spectral feature important maps for various classes.

In this work, we combined Raman spectroscopy and machine learning to develop an approach to rapidly screen AD biomarkers **(Figure 1)**. Specifically, we collected Raman spectra on mice brain slices with and without AD. Our Raman measurements suggest that the signal-to-noise ratios and the subsequent machine learning classification performance can be effectively improved by using monolayer graphene in contact with mouse brain slices. By comparing the machine learning prediction accuracy on Raman spectra from different brain regions, our experiment revealed that certain brain regions, such as cortex, are more informative in AD identification. Beyond using machine learning for AD/non-AD classification, we also interpreted the machine learning results by obtaining Raman spectral feature importance maps. Since Raman spectra are molecular fingerprints, such important feature ranges are found to register well with the Raman feature ranges of known AD biomarkers including Aβ and tau proteins. In addition, we discovered several other molecules that have high spectral correlation with the important feature ranges, indicating their potential as the biomarkers for AD diagnosis. To the best of our knowledge, this work is the first to employ Raman spectral features and machine learning with feature importance to analyze AD brains down to the molecular level. Our interpretable machine learning based framework provides a route for fundamental study of AD pathology and can greatly accelerate AD biomarker discovery, diagnosis, and drug development.

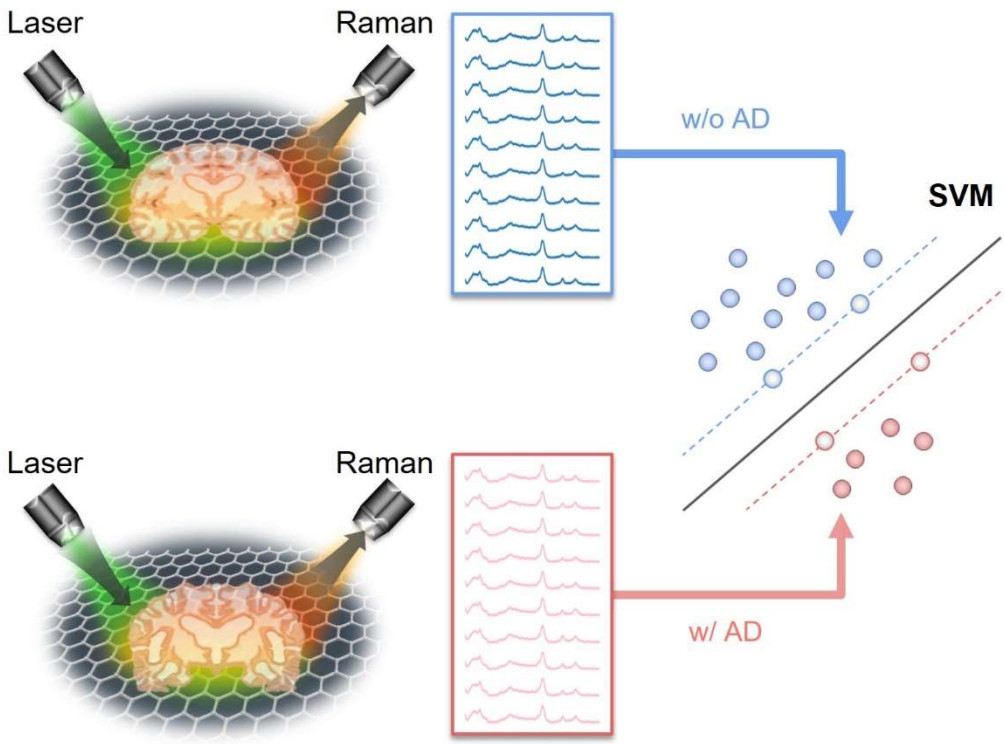

Figure 1. The overall workflow. Workflow of graphene-assisted Raman signals data collection, preparation, classification. The machine learning classifier demonstrated is the linear SVM model to differentiate AD/non-AD Raman spectra.

2. Results

2.1. Dataset

We collected Raman spectra on brain slices harvested from four types of mice: sample 1 (non-AD, 14 months of age), sample 2 (AD, 14 months), sample 3 (non-AD, 4 months), and sample 4 (AD, 4 months). Tables S1 and S2 provide the complete information of brain slice and Raman spectra. There are in total 727 Raman spectra in our dataset. The Raman measurements were performed on 5-8 brain slices for each category. On each brain slice, we performed Raman measurement on 3 brain regions: cortex, hippocampus, and thalamus. The brain slices were immersed in neuroprotectant solution sealed between the silicon substrate and a fused quartz cover slide. For part of the measurements, we also placed brain slices in direct contact with monolayer graphene which was transferred on the quartz cover slide (Figure S1). In total, 27 Raman spectra were measured on each brain region with or without graphene.

2.2. Preprocessing and Calculating Signal-to-Noise Ratio

Before feeding the Raman spectra into machine learning classifiers, we implemented the Savitzky-Golary filter[29] for spectral smoothing and asymmetric least squares smoothing[30] for baseline correction. An example of raw Raman spectrum before and after preprocessing is shown in **Figure 2**a.

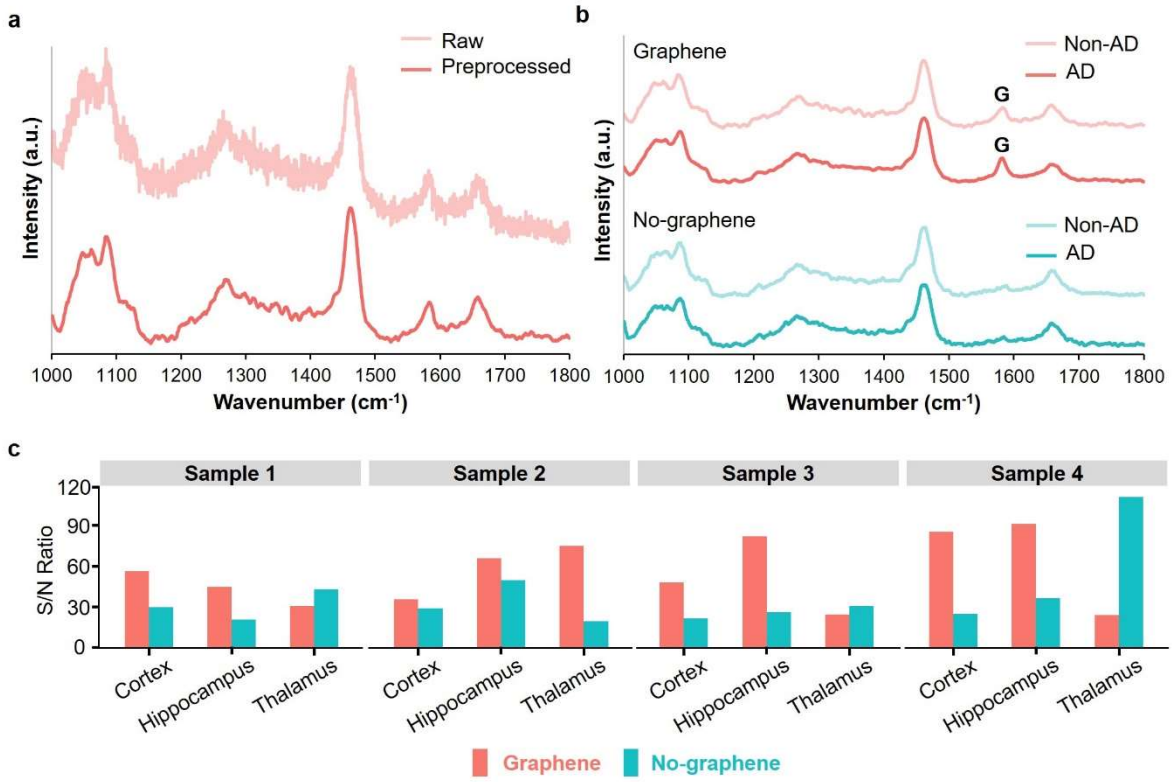

Figure 2. Raman spectra on brain slices and S/N. (a) Graphene-assisted Raman spectra of AD sample in cortex region before and after preprocessing measured. (b) Preprocessed Raman spectra in cortex region with and without AD, with and without graphene. Graphene G-band signal at 1589 cm^{-1} is notated as "G". (c) S/N of all samples in every brain region and measured with and without graphene.

We calculated signal-to-noise ratios (S/N) for spectra with and without graphene in all brain regions. For graphene-assisted Raman spectra, we excluded the graphene G-band at 1589 cm^{-1} (Figure 2b). The S/N are shown in Figure 2c where red bars correspond to graphene-assisted spectra excluding the graphene G-band signal and blue bars represent the no-graphene results. It is clear that the graphene-assisted spectra exhibit much higher S/N than the no-graphene spectra do for among almost all the samples and brain regions (S/N average of 56.0 for graphene-assisted spectra compared to 37.1 for no-graphene spectra). The only exceptions are thalamus

regions of sample 1, sample 3 and sample 4 where the no-graphene spectra have slightly better S/N (43.3, 30.8, 113.0 for no-graphene spectra, compared to 30.9, 24.6, 24.3 for graphene-assisted spectra, for the three samples respectively). Overall, we observed that when placed in contact with graphene, the brain slice samples exhibit less noise when compared to the measurements when mice brain slices are not in contact with graphene.

Our prior work, along with others, has shown that graphene can reduce noise of Raman spectra, enhance Raman signals, and quench fluorescence for organic and biomolecules[31–34]. Here, our observation of reduced noise is partially due to the high heat conductivity of graphene which can reduce the laser heating effect during Raman measurements of brain slices. Therefore, we used graphene-assisted Raman spectra for further investigation in the following sections.

2.3. Machine Learning Classification

As proven in Figure 2c, the S/N for Raman spectra measured with graphene is effectively increased, hence in our machine learning analysis, we used the graphene-assisted spectra and applied different algorithms including Linear SVM[26], random forest[27], XGBoost[35], CatBoost[36]. The classification accuracy, area under the receiver operating characteristic curve (AUC), sensitivity, and specificity for graphene-assisted Raman spectra are shown in **Figure 3**. The four metrics are common metrics for machine learning classifiers. Although the Raman spectra for AD and non-AD samples are visually similar (Figure 2b), machine learning classification can differentiate the two classes with high accuracy. It can be seen from Figure 3 that the cortex region rendered the accuracy over 93% for every classifier. Compared to two other brain regions hippocampus and thalamus, cortex region exhibits better accuracy, AUC, sensitivity, and specificity for all classifiers. Thus, we can infer that cortex is an informative brain region with AD-relevant biomarkers[37], which can be easily captured by Raman spectroscopy. It should be noted that our results do not indicate that the roles of hippocampus and thalamus in AD should be ignored, since our observations only indicate that Raman is more sensitive to AD-relevant molecular components in the cortex region compared to the other two regions. We also performed the same machine learning classification for Raman spectra measured without graphene, and the results are shown in Figure S2.

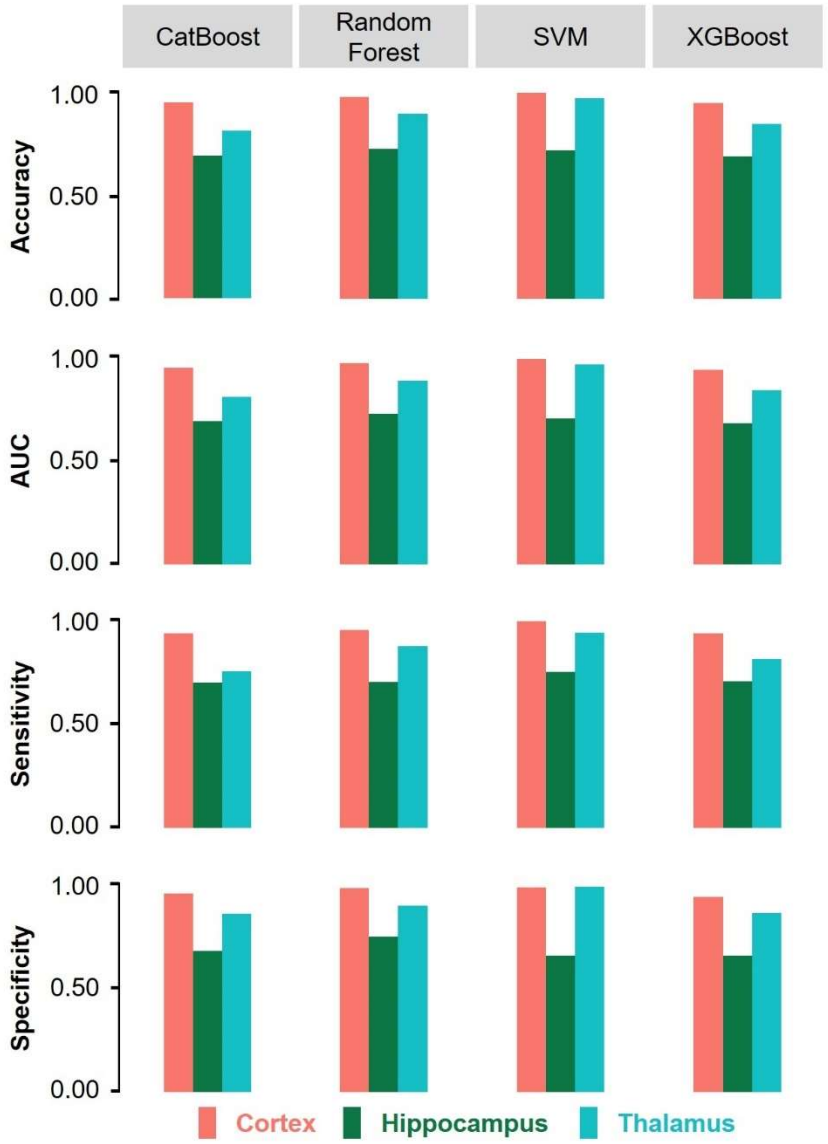

Figure 3. Machine learning classification on graphene-assisted Raman spectra. Accuracy, AUC, sensitivity, and specificity of graphene-assisted Raman spectra from cortex, hippocampus and thalamus regions of all brain samples.

Having established that graphene-assisted Raman signals from the cortex region are more desirable for machine learning, we visualized its data distribution for insights into selecting appropriate interpretable machine learning classifiers in the format of t-distributed stochastic neighbor embedding (t-SNE) plots, a non-linear dimensionality reduction technique developed to embed high-dimensional data for visualization in a low-dimensional space[38]. As shown in **Figure 4**a, in the cortex region, the graphene-assisted Raman data can be well separated by a

linear decision boundary while the Raman data measured without graphene are apparently not linearly separable (Figure 4b). Meanwhile, the machine learning classification accuracy using graphene-assisted Raman data reaches as high as 98% using SVM (Figure 4c); however, the accuracy is at most 77% among the four classifiers using the no-graphene data (Figure 4c). This, again, shows the high quality of our graphene-assisted Raman data, which are more suitable for spectral feature importance analysis and interpretation (t-SNE plots from other brain regions are in Figure S3). To perform this interpretation task, a linear classifier is preferable since it is simple yet sufficient to fit the linearly-separated data without introducing much model complexity, making its spectral feature map more straightforward for interpretation. Thus, from the series of machine learning models experimented, we chose linear SVM for further investigation to determine candidate biomarkers in association with AD.

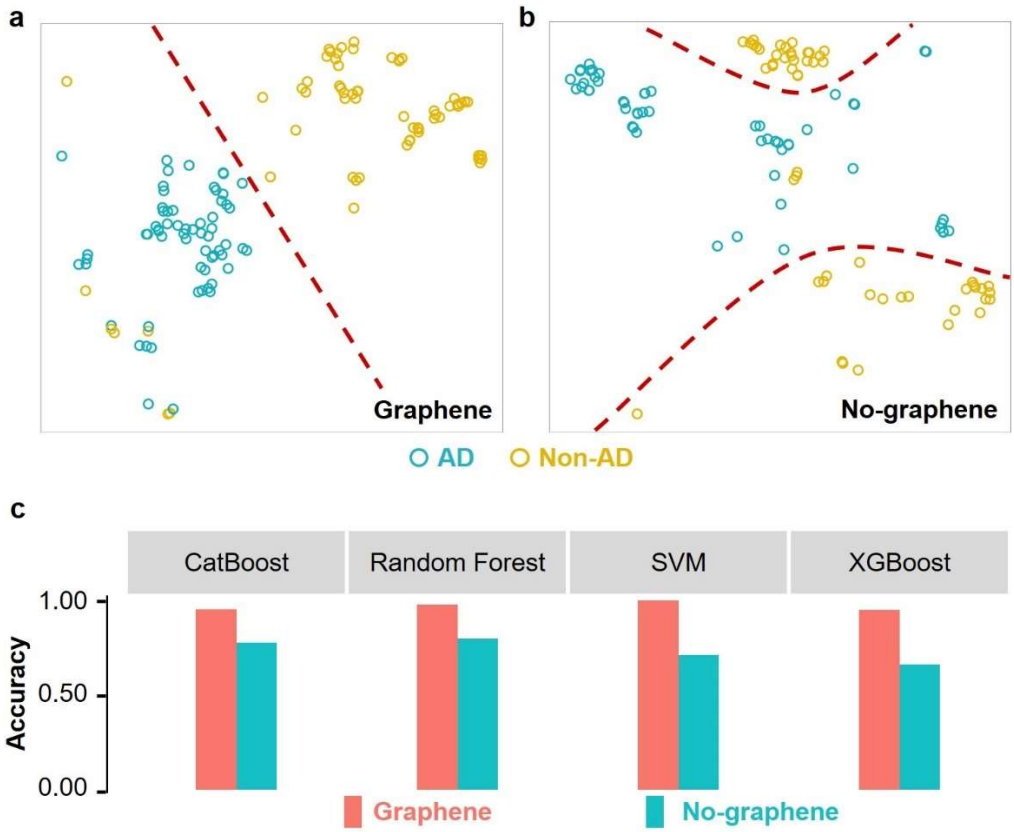

Figure 4. t-SNE plots for cortex region. (a) t-SNE plot of graphene-assisted spectra on cortex region. The red dash line is the estimated linear decision boundary. (b) t-SNE plot of spectra without graphene on cortex region. The red dash curves are estimated non-linear decision boundaries. (c) Comparison of classification accuracy between Raman spectra with and without graphene on cortex region.

2.4. Machine Learning Interpretation

Next, we further interpreted the machine learning classification results and studied the features learned, which can provide important information of AD biomarker molecules. Validated by high accuracy, AUC, sensitivity and specificity (Figure 3), the features learned by SVM on the graphene-assisted data in the cortex region are considered reliable for interpretation. We assigned a score map of Raman features based on their importance in classification of AD/non-AD. The extracted feature importance map contains two sets of features: positive features and negative features (positive features shown in **Figure 5**, and complete features shown in Figure S4).

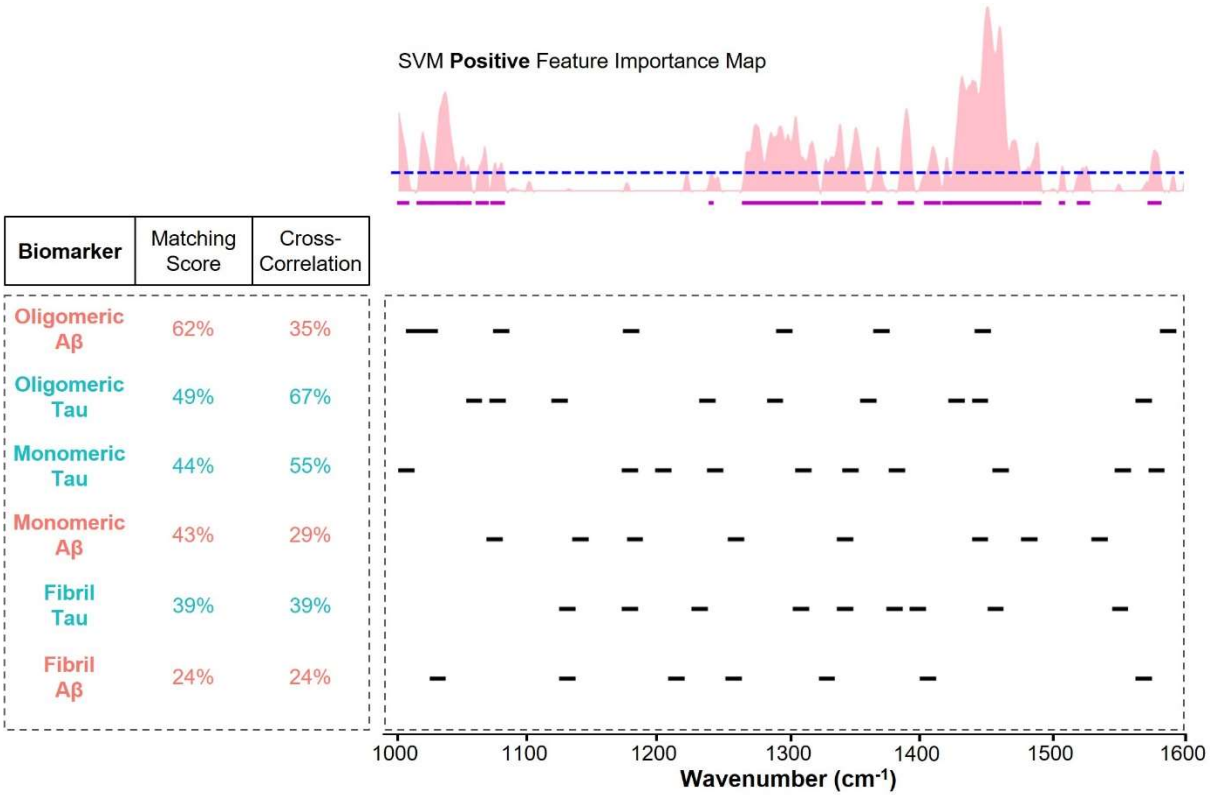

Figure 5. Feature importance matching for AD biomarkers. (Top) The positive feature importance map found by SVM, where wavenumbers with high feature importance scores (i.e. high values along vertical axis) are important for AD recognition. On the feature importance map, the blue dash line is the threshold of positive important feature ranges used for frequency matching score. The purple solid lines are important feature ranges over the threshold. (Bottom left) The matching scores and cross correlation coefficients between SVM feature importance map and previously reported 6 biomarkers. (Bottom right) The black solid lines below the feature importance map are Raman signature peak ranges of 6 biomarkers with plus/minus 5 cm^{-1}. The wavenumber ranges from 1000 to 1600 cm^{-1}.

To better understand our spectral feature importance map and its relationship with molecular components, we developed two metrics for two application scenarios: Pearson cross-correlation based algorithm (if Raman spectra of biomarkers, including peak frequencies and intensities, are available), and matching score based on spectral overlap between important feature ranges and biomarker Raman peaks (if only the peak frequencies of biomarkers are known, and peak intensities are unavailable). Note that the latter metric is robust, since the Raman peak frequencies are relatively more robust while the intensities are complicated and can depend on various measurement conditions such as laser wavelength, laser power, and substrate. Thus, here we used both metrics to cross check our interpretation results. We first examined several major AD biomarker proteins using both metrics. From the results shown in Figure 5, it is obvious that the known AD biomarkers such as oligomeric tau (with Raman peaks at 1056, 1288, 1428, 1446 cm^{-1}, etc.) and oligomeric Aβ (with Raman peaks at 1077, 1295, 1448 cm^{-1}, etc.) have considerable cross-correlation coefficients (Metric #1) and matching scores (Metric #2). This demonstrates the validity of our metrics.

Using these metrics, we can discover more molecules that are potentially correlated to AD. We applied matching score and cross-correlation coefficient to 17 major composite molecules of the brain (Table S3). The spectra of the component molecules with cross-correlation coefficients above 0.65 are shown in **Figure 6**. Triolein, phosphatidylcholine, and actin have the highest cross-correlation to feature importance map of 72%, 71%, 69%, respectively. Consistent with the cross-correlation metric, the matching scores of these three molecules are also the highest among the 17 composite molecules. As clearly seen in Figure 6, these components all consist of strong Raman peaks in ranges 1270 – 1380 cm^{-1} and 1400 – 1500 cm^{-1}, which are the two most important feature ranges identified by our SVM classifier. This suggests that triolein, phosphatidylcholine and actin may be associated with AD, which have been experimentally validated by several prior reports through biochemical and physiological studies[39–41].

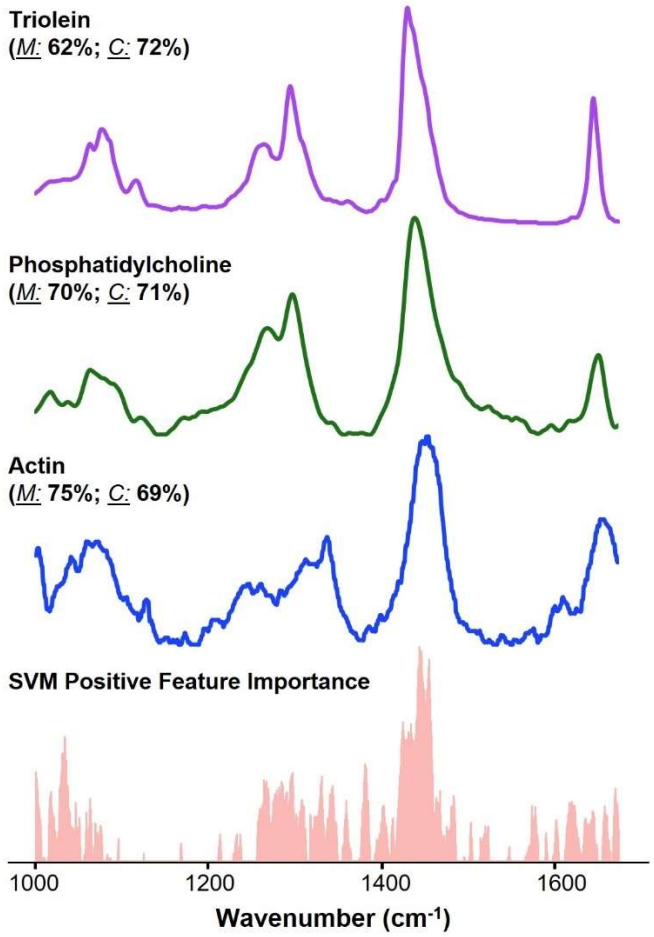

Figure 6. Other potential AD biomarkers identified. Biomolecular component spectra with the top 3 cross-correlation coefficients to the feature importance map: triolein, phosphatidylcholine and actin. *M* refers to the matching score, and *C* refers to the cross-correlation coefficient.

In addition to the positive features shown in Figures 5 and 6, the SVM classifier also finds negative features in the range 1100-1220 cm^{-1}, i.e., the representative Raman spectral range for non-AD brain samples (Figure S4). This means that biomolecules with Raman peaks in this wavenumber range tend to be negatively correlated with AD (i.e. they likely reduce in amount or disappear with AD). These negative features correspond to cytochrome and glycogen in both matching metrics, suggesting that cytochrome and glycogen are negatively correlated to AD, again consistent with prior biochemical experiments[42–45].

3. Discussion

Our work clearly demonstrates the effectiveness of employing supervised machine learning to classify graphene-assisted Raman spectra of mice brain slices. Our approach also provides both positive and negative feature importance maps that can correlate to specific brain molecules. Overall, our analysis on known biomarkers validated that our machine learning algorithm with matching technique is capable of detecting Raman signals that are related to AD. Further, we analyzed other common molecular components in brain, and found potentially new biomarkers including triolein, phosphatidylcholine and actin.

Our correlation analyses showed that triolein, phosphatidylcholine and actin are associated with AD. This result is also supported by other experimental works. For example, Bamburg et al. found the increase of actin in AD brain compared to normal brain[39]. Johnson et al. suggested that triglycerides, including triolein, can also lead to cognitive impairments and that switching to a low-fat diet feeding in mice can recover cognitive function[46]. Banks et al. showed that the decrease of triglycerides, including triolein, improves both learning and memory capabilities[40]. High levels of phosphatidylcholine usually reduce the progression of dementia in people with AD[47]. Phosphatidylcholine is also found to be significantly lower in AD patients[48]. However, AD pathogenesis is different in mice and human brains regarding phosphatidylcholine levels. According to Chan et al., phosphatidylcholine levels are lower in AD human brain while higher in mouse forebrain[41]. Thus, our results correctly showed the positive correlation between phosphatidylcholine and AD in mice.

Cytochrome and glycogen were found to be important in non-AD samples in our results. In earlier studies, glycogen has been purposed to have beneficial effects for the brain. Storage of glycogen is associated with cognition and therefore, contributes to non-AD[42]. The significant role and effect of glycogen on AD are also confirmed by Bass et al.[43]. Cytochrome has also been found decreased in AD samples. For example, cytochrome c oxidase is found decreased in AD as reported by Parker et al. and Cardoso et al[44,45].

We also noted that our approach is able to provide a screening of potential biomarkers, rather than to accurately pinpoint all the biomarkers. Our component matching score metrics depend on the quality and range of components in Raman signals. However, the Raman signal range used was 1000 – 1600 cm^{-1}. Significant signals that are not in this range could modify matching scores of Aβ and tau proteins in our analysis. Besides, in this work, the biomarker matching was performed for the 17 common brain molecules with known Raman spectra. However, our method in principle has no limit in the number of biomarkers to screen. To identify more potential biomarkers, we simply need to use the Raman spectra of other biomolecules (e.g. from a Raman spectra database) in our component matching with feature importance spectra.

In summary, we measured and analyzed Raman spectra on mice brain slices with and without AD, and used machine learning to classify AD/non-AD spectra and discover biomarkers through

spectral feature interpretation. We implemented graphene-assisted Raman measurements and found that monolayer graphene can enhance Raman S/N, and thus can effectively improve the performance of machine learning classification to achieve a high accuracy of 98%. We studied different brain regions, and found that the cortex is a more informative region with Raman spectral signatures. In addition, we obtained spectral feature importance maps based on our machine learning classifier, and developed two new metrics, cross-correlation and matching score coefficient, to identify molecules that are relevant to AD. Our interpretable machine learning based framework recognizes that known AD biomarkers such as oligomeric tau and oligomeric Aβ have considerable correlation to AD. Our model also identifies three molecules (triolein, phosphatidylcholine and actin) that are positively correlated to AD, and two molecules (cytochrome and glycogen) that are negatively correlated to AD. Our work offers a rapid approach to detect AD and to screen AD biomarker molecules, thus is promising to greatly accelerate the study of AD in terms of diagnosis and treatment. Our approach integrating graphene-assisted Raman spectroscopy and interpretable machine learning can also be widely applied to study a variety of other diseases.

4. Methods

4.1. Animals and brain slice preparation

Animal investigation procedures were conducted in accordance with institutional and NIH guidelines. The animals were housed with *ad libitum* access to food and water in a room with a 12-hr light and dark cycle in the animal facility. We utilized the previously reported 5XFAD mouse model expressing $APP^{Swedish/Florida/London}$ and $PSEN1^{M146L/\ L286V}$ mutations[49,50], which recapitulates the features of Alzheimer's β-amyloid pathology in animal brains. 5XFAD mice of different ages and non-transgenic (non-AD) control mice were investigated. All animal study procedures were approved by MGH IACUC (Protocol #: 2011N000022).

Brain slices were prepared following previously reported methods[51,52]. Particularly, animals were anesthetized with isoflurane and then decapitated. Isolated brains were longitudinally bisected, and hemispheres were separated and incubated in 4% paraformaldehyde-containing 0.1 M phosphate-buffered saline (PBS) at 4 ºC for 48 hrs, followed by incubation in 30% sucrose solution in 0.1 M PBS. Next, brains were snap frozen from a dry ice-cooled block on a sliding microtome (Leica SM 2010R), and sectioned in 40 μm thickness. The free-floating brain sections were stored at −20°C in a cryoprotective buffer containing 28% ethylene glycol, 23% glycol, and 0.05 M PBS, until subsequent analysis by Raman testing.

4.2. Raman measurement

The Raman measurement was performed on Horiba LabRam system with 50× objective. The laser power on the sample was controlled below 0.4 mW to avoid potential laser bleaching.

Excitation laser wavelength was 532.5 nm. All the measurements were performed on mice brain slices in the neuroprotectant solution that was sealed between a quartz cover slide and the silicon substrate. In the case with graphene in contact, the quartz slide has monolayer graphene transferred on the surface.

4.3. Graphene synthesis and transfer

The graphene layers were synthesized by chemical vapor deposition method. For the graphene growth, Cu foil was first placed in a quartz tube furnace and annealed at 1065°C for 1hr under 60 sccm H_2 and 940 sccm Ar at atmospheric pressure. For the growth, the furnace was brought down to 1000°C and the gas flow rates were updated to 36 sccm H_2 and 2204 sccm Ar. Then 0.6 sccm CH_4 was introduced for 1hr. After 1hr, the CH_4 was turned off and the Cu foil was rapidly cooled by removing it from the furnace area.

For the transfer, a supporting PMMA layer was spin-coated on top of the graphene/Cu stack. Then the Cu was etched away using commercial Cu etchant. After the Cu has etched, the PMMA/graphene was put into three separate water baths for several hours, before being transferred to the desired final substrate. After the sample has dried, it was placed into acetone overnight in order to remove the PMMA and then rinsed with isopropyl alcohol and blow dried.

4.4. Data preprocessing and calculation of signal-to-noise ratio

After obtaining the raw data, it is essential to apply preprocessing methods to reduce the effect of noise and background on classifiers. For each spectrum, we applied Savitzky-Golary filter to reduce the spectral noise[29]. We removed the background using baseline correction with asymmetric least squares smoothing[30]. To calculate S/N, we estimated the noise by using standard deviation of difference spectra from same brain region of the same sample. Then, we used signal-to-noise built in function in MATLAB to calculate the S/N for every spectra of every brain region under every measuring condition (graphene, no-graphene). Finally, we averaged the S/N for all the spectra in each region.

4.5. Classifiers architecture and feature importance

As shown in Figure 3, multiple classifiers were used in the experiment including linear SVM, random forest, XGBoost, and CatBoost. Classification experiments were implemented using stratified 5-fold cross validation to preserve the same percentage of samples for each class to improve robustness. For experiments with a relatively small sample set, SVM is usually an efficient while reliable option, for it is designed to find the optimal decision boundary as represented by a hyperplane that maximizes the margin of separation between different classes[53]. In our binary classification, we used linear SVM to find the optimal linear decision boundary between the two classes. The sign of a feature weight obtained from the Linear SVM classifier represents that feature's direction to predict class[54,55]. Hence, the feature weights can be intuitively interpreted as feature importance map shown in Figure 5 (positive only), while the

positive (negative) features correspond to Raman signals more represented in AD (non-AD) samples. We used scikit-learn package to implement linear SVM and extract feature importance map[56].

4.6. Component Cross-correlation Coefficient for Raman

Pearson correlation coefficient measures the linear correlation between two variables[57]. The method is a standard measure of similarity between two Raman spectra[58]. Here, we used the cross-correlation coefficient to measure the levels of correlation between the machine-learning derived feature maps and the Raman spectra of 17 commonly known components in brain from literature (Table S3)[59–74]. We modified the Pearson correlation coefficient method and excluded negatively correlated trends as shown as follows:

$$r_{xy} = \frac{\sum_{i=0}^{n} \max\big(0, (x_i - \bar{x})(y_i - \bar{y})\big)}{\sqrt{\sum_{i=0}^{n}(x_i - \bar{x})^2}\sqrt{\sum_{i=0}^{n}(y_i - \bar{y})^2}} \tag{1}$$

Considering the range difference of each spectrum, we normalized the components' spectra and the feature importance map so that they were within the same interval (1000 – 1600 cm^{-1}) and have the same dimension. Then we used *Equation 1* to calculate the cross-correlation coefficient. This results a coefficient that ranges from [0,1] where *r=0* means no correlation and *r=1* means perfect correlation.

4.7. Matching Score Between Machine-learning derived Feature Map and Biomolecule Raman Spectra

Raman peak intensities vary with a number of factors including excitation wavelength and substrate. To avoid the influence of Raman peak intensity variation, we developed another metric, the *Matching Score,* for measuring the correlation between biomarkers and distinguishable patterns learned from machine learning models to some extent. The metric is designed as a ratio, with the numerator as the sum of important feature ranges of the extracted feature map of a particular class (i.e. either AD or No AD) that overlap with Raman spectra peak ranges of a certain biomarker, the sum of the aforementioned biomarker peak ranges is used as the denominator. Significant Raman peak ranges of 6 biomarkers (Fibril tau, Fibril Aβ, Oligomeric tau, Oligomeric Aβ, Monomeric tau and Monomeric Aβ) that are commonly known to be present in brain slides are gathered from literature[75–77]. As demonstrated in Figure 5, Raman peak ranges are constructed by granting a shift of 5 wavenumbers for each biomarker representing important feature regions, the sum of which is utilized as the denominator for further calculations. Similarly, pinpointing the important feature ranges for the feature maps as numerator is also desired. Rather than extracting peaks from feature maps, we applied a 40% percentile threshold as the cutoff, regions above which we considered as significant and used the sum of their intersection with the denominator as the numerator. Matching scores of all six biomarkers and the positive feature map extracted from Linear SVM training are presented in

Figure 5, indicating that results from our *Matching Score* approach is consistent with biomedical findings using other methods.

Supporting Information

The Supporting Information is available online.

Acknowledgments

The authors thank the Imaging Facility of Materials Characterization Lab at Penn State for instrument use. C.Z. and S.H. acknowledge the support from the National Institutes of Health under grant number R56AG062208. L.D. and S.H. acknowledge the support from Johnson & Johnson Inc. for the STEM2D Scholar's Award. S.H. acknowledges the support from the National Science Foundation under grant number ECCS-1943895. C.Z. acknowledges the support from the National Institutes of Health under grant number R01AG055784. C.Z. and R.E.T. acknowledge the support from the Cure Alzheimer's Fund.

Conflict of Interest

Authors declare that they have no competing interests.

Author Contributions

Z.W., J.Y., and L.D. performed experiments and analyzed data. T.G-N. and M.T. synthesized graphene. S.S. and I.B. helped with data analysis. S.H.C., C.R., R.E.T., and C.Z. prepared the brain samples. S.X.H., C.Z., and S.H. designed and supervised the work. Z.W. and J.Y. wrote the manuscript draft and prepared the figures. All authors reviewed and revised the manuscript to its final state.

References

[1] A. Burns, *BMJ* **n.d.**, *338*, 467.

[2] C. Sawda, C. Moussa, R. S. Turner, *Ann. N. Y. Acad. Sci.* **2017**, *1403*, 142.

[3] B. Olsson, R. Lautner, U. Andreasson, A. Öhrfelt, E. Portelius, M. Bjerke, M. Hölttä, C. Rosén, C. Olsson, G. Strobel, E. Wu, K. Dakin, M. Petzold, K. Blennow, H. Zetterberg, *Lancet Neurol.* **2016**, *15*, 673.

[4] K. Blennow, H. Zetterberg, *J. Intern. Med.* **2018**, *284*, 643.

[5] H. Zetterberg, B. B. Bendlin, *Mol. Psychiatry* **2021**, *26*, 296.

[6] P. Chen, A. Shen, W. Zhao, S.-J. Baek, H. Yuan, J. Hu, *Appl. Opt.* **2009**, *48*, 4743.

[7] F. Márquez, M. A. Yassa, *Mol. Neurodegener.* **2019**, *14*, 21.

[8] J. L. Molinuevo, S. Ayton, R. Batrla, M. M. Bednar, T. Bittner, J. Cummings, A. M. Fagan, H. Hampel, M. M. Mielke, A. Mikulskis, S. O'Bryant, P. Scheltens, J. Sevigny, L. M. Shaw, H. D. Soares, G. Tong, J. Q. Trojanowski, H. Zetterberg, K. Blennow, *Acta Neuropathol.* **2018**, *136*, 821.

[9] L. Shi, L. Lu, G. Harvey, T. Harvey, A. Rodríguez-Contreras, R. R. Alfano, *Sci. Rep.* **2017**, *7*, 2599.

[10] J. Shin, S. Park, H. Lee, Y. Kim, *Sci. Rep.* **2021**, *11*, 1617.

[11] Y. W. Jun, S. W. Cho, J. Jung, Y. Huh, Y. Kim, D. Kim, K. H. Ahn, *ACS Cent Sci* **2019**, *5*, 209.

[12] P. S. Aisen, *J Prev Alzheimers Dis* **2019**, *6*, 150.

[13] J. Langer, D. Jimenez de Aberasturi, J. Aizpurua, R. A. Alvarez-Puebla, B. Auguié, J. J. Baumberg, G. C. Bazan, S. E. J. Bell, A. Boisen, A. G. Brolo, J. Choo, D. Cialla-May, V. Deckert, L. Fabris, K. Faulds, F. J. García de Abajo, R. Goodacre, D. Graham, A. J. Haes, C. L. Haynes, C. Huck, T. Itoh, M. Käll, J. Kneipp, N. A. Kotov, H. Kuang, E. C. Le Ru, H. K. Lee, J.-F. Li, X. Y. Ling, S. A. Maier, T. Mayerhöfer, M. Moskovits, K. Murakoshi, J.-M. Nam, S. Nie, Y. Ozaki, I. Pastoriza-Santos, J. Perez-Juste, J. Popp, A. Pucci, S. Reich, B. Ren, G. C. Schatz, T. Shegai, S. Schlücker, L.-L. Tay, K. G. Thomas, Z.-Q. Tian, R. P. Van Duyne, T. Vo-Dinh, Y. Wang, K. A. Willets, C. Xu, H. Xu, Y. Xu, Y. S. Yamamoto, B. Zhao, L. M. Liz-Marzán, *ACS Nano* **2020**, *14*, 28.

[14] M. Ikejiri, M. Oba, T. Ito, R. Wen, T. Mizutani, K. Misawa, in *14th Pacific Rim Conference on Lasers and Electro-Optics (CLEO PR 2020)*, Optical Society Of America, **2020**, p. P3_18.

[15] S. Khan, R. Ullah, A. Khan, R. Ashraf, H. Ali, M. Bilal, M. Saleem, *Photodiagnosis Photodyn. Ther.* **2018**, *23*, 89.

[16] M. Jermyn, J. Desroches, J. Mercier, M.-A. Tremblay, K. St-Arnaud, M.-C. Guiot, K. Petrecca, F. Leblond, *J. Biomed. Opt.* **2016**, *21*, 94002.

[17] S. Laing, L. E. Jamieson, K. Faulds, D. Graham, *Nature Reviews Chemistry* **2017**, *1*, 0060.

[18] M. Paraskevaidi, C. L. M. Morais, D. E. Halliwell, D. M. A. Mann, D. Allsop, P. L. Martin-Hirsch, F. L. Martin, *ACS Chem. Neurosci.* **2018**, *9*, 2786.

[19] M. Ji, M. Arbel, L. Zhang, C. W. Freudiger, S. S. Hou, D. Lin, X. Yang, B. J. Bacskai, X. S. Xie, *Sci Adv* **2018**, *4*, eaat7715.
[20] B. Lochocki, T. H. J. Morrema, F. Ariese, J. J. M. Hoozemans, J. F. de Boer, *Analyst* **2020**, *145*, 1724.
[21] S. Li, Y. Zhang, J. Xu, L. Li, Q. Zeng, L. Lin, Z. Guo, Z. Liu, H. Xiong, S. Liu, *Appl. Phys. Lett.* **2014**, *105*, 091104.
[22] S. Khan, R. Ullah, S. Shahzad, N. Anbreen, M. Bilal, A. Khan, *Photodiagnosis Photodyn. Ther.* **2018**, *24*, 286.
[23] W. R. da Silva, L. Silveira Jr, A. B. Fernandes, *Lasers Med. Sci.* **2020**, *35*, 1065.
[24] C. Chen, L. Yang, J. Zhao, Y. Yuan, C. Chen, J. Tang, H. Yang, Z. Yan, H. Wang, X. Lv, *Optik* **2020**, *203*, 164043.
[25] A. Stefancu, M. Badarinza, V. Moisoiu, S. D. Iancu, O. Serban, N. Leopold, D. Fodor, *Anal. Bioanal. Chem.* **2019**, *411*, 5877.
[26] Y. Zhang, in *Information Computing and Applications*, Springer Berlin Heidelberg, **2012**, pp. 179–186.
[27] L. Breiman, *Mach. Learn.* **2001**, *45*, 5.
[28] A. Lapedes, R. Farber, in *Evolution, Learning and Cognition*, WORLD SCIENTIFIC, **1989**, pp. 331–346.
[29] A. Savitzky, M. J. E. Golay, *Anal. Chem.* **1964**, *36*, 1627.
[30] P. H. C. Eilers, H. F. M. Boelens, *Leiden University Medical Centre Report* **2005**, *1*, 5.
[31] S. Huang, X. Ling, L. Liang, Y. Song, W. Fang, J. Zhang, J. Kong, V. Meunier, M. S. Dresselhaus, *Nano Lett.* **2015**, *15*, 2892.
[32] A. Silver, H. Kitadai, H. Liu, T. Granzier-Nakajima, M. Terrones, X. Ling, S. Huang, *Nanomaterials (Basel)* **2019**, *9*, DOI 10.3390/nano9040516.
[33] X. Ling, S. Huang, S. Deng, N. Mao, J. Kong, M. S. Dresselhaus, J. Zhang, *Acc. Chem. Res.* **2015**, *48*, 1862.
[34] S. Huang, R. Pandey, I. Barman, J. Kong, M. Dresselhaus, *ACS Photonics* **2018**, *5*, 2978.
[35] T. Chen, C. Guestrin, in *Proceedings of the 22nd ACM SIGKDD International Conference on Knowledge Discovery and Data Mining*, Association For Computing Machinery, New York, NY, USA, **2016**, pp. 785–794.
[36] L. Prokhorenkova, G. Gusev, A. Vorobev, A. V. Dorogush, A. Gulin, *arXiv [cs.LG]* **2017**.
[37] K. Hensley, N. Hall, R. Subramaniam, P. Cole, M. Harris, M. Aksenov, M. Aksenova, S. P. Gabbita, J. F. Wu, J. M. Carney, *J. Neurochem.* **1995**, *65*, 2146.
[38] L. van der Maaten, "Visualizing Data using t-SNE," can be found under https://www.jmlr.org/papers/volume9/vandermaaten08a/vandermaaten08a.pdf?fbclid=IwAR0Bgg1eA5TFmqOZeCQXsIoL6PKrVXUFaskUKtg6yBhVXAFFvZA6yQiYx-M, **2008**.
[39] J. R. Bamburg, B. W. Bernstein, *Cytoskeleton* **2016**, *73*, 477.
[40] W. A. Banks, S. A. Farr, T. S. Salameh, M. L. Niehoff, E. M. Rhea, J. E. Morley, A. J. Hanson, K. M. Hansen, S. Craft, *Int. J. Obes.* **2018**, *42*, 391.

[41] R. B. Chan, T. G. Oliveira, E. P. Cortes, L. S. Honig, K. E. Duff, S. A. Small, M. R. Wenk, G. Shui, G. Di Paolo, *J. Biol. Chem.* **2012**, *287*, 2678.
[42] M. Bélanger, I. Allaman, P. J. Magistretti, *Cell Metab.* **2011**, *14*, 724.
[43] B. Bass, S. Upson, K. Roy, E. L. Montgomery, T. O. Jalonen, I. V. J. Murray, *Neural Regeneration Res.* **2015**, *10*, 1023.
[44] W. D. Parker Jr, C. M. Filley, J. K. Parks, *Neurology* **1990**, *40*, 1302.
[45] S. M. Cardoso, M. T. Proença, S. Santos, I. Santana, C. R. Oliveira, *Neurobiol. Aging* **2004**, *25*, 105.
[46] L. A. Johnson, K. L. Zuloaga, T. L. Kugelman, K. S. Mader, J. T. Morré, D. G. Zuloaga, S. Weber, T. Marzulla, A. Mulford, D. Button, J. R. Lindner, N. J. Alkayed, J. F. Stevens, J. Raber, *EBioMedicine* **2016**, *3*, 26.
[47] J. P. Higgins, L. Flicker, *Cochrane Database Syst. Rev.* **2000**, CD001015.
[48] L. Whiley, A. Sen, J. Heaton, P. Proitsi, D. García-Gómez, R. Leung, N. Smith, M. Thambisetty, I. Kloszewska, P. Mecocci, H. Soininen, M. Tsolaki, B. Vellas, S. Lovestone, C. Legido-Quigley, AddNeuroMed Consortium, *Neurobiol. Aging* **2014**, *35*, 271.
[49] H. Oakley, S. L. Cole, S. Logan, E. Maus, *Journal of* **2006**.
[50] K. L. Youmans, L. M. Tai, T. Kanekiyo, W. B. Stine Jr, S.-C. Michon, E. Nwabuisi-Heath, A. M. Manelli, Y. Fu, S. Riordan, W. A. Eimer, L. Binder, G. Bu, C. Yu, D. M. Hartley, M. J. LaDu, *Mol. Neurodegener.* **2012**, *7*, 8.
[51] Y. Liang, F. Raven, J. F. Ward, S. Zhen, S. Zhang, H. Sun, S. J. Miller, S. H. Choi, R. E. Tanzi, C. Zhang, *J. Alzheimers. Dis.* **2020**, *76*, 1071.
[52] S. H. Choi, E. Bylykbashi, Z. K. Chatila, S. W. Lee, B. Pulli, G. D. Clemenson, E. Kim, A. Rompala, M. K. Oram, C. Asselin, J. Aronson, C. Zhang, S. J. Miller, A. Lesinski, J. W. Chen, D. Y. Kim, H. van Praag, B. M. Spiegelman, F. H. Gage, R. E. Tanzi, *Science* **2018**, *361*, DOI 10.1126/science.aan8821.
[53] S. Li, Z. Guo, Z. Liu, *Expert Rev. Anticancer Ther.* **2015**, *15*, 5.
[54] T. Howley, M. G. Madden, M.-L. O'Connell, A. G. Ryder, in *Applications and Innovations in Intelligent Systems XIII*, Springer London, **2006**, pp. 209–222.
[55] A. J. Smola, B. Schölkopf, *Learning with Kernels*, Citeseer, **1998**.
[56] L. Buitinck, G. Louppe, M. Blondel, F. Pedregosa, A. Mueller, O. Grisel, V. Niculae, P. Prettenhofer, A. Gramfort, J. Grobler, R. Layton, J. Vanderplas, A. Joly, B. Holt, G. Varoquaux, *arXiv [cs.LG]* **2013**.
[57] J. Benesty, J. Chen, Y. Huang, I. Cohen, in *Noise Reduction in Speech Processing* (Eds.: I. Cohen, Y. Huang, J. Chen, J. Benesty), Springer Berlin Heidelberg, Berlin, Heidelberg, **2009**, pp. 1–4.
[58] T. Roliński, S. Gawinkowski, A. Kamińska, J. Waluk, in *Optical Spectroscopy and Computational Methods in Biology and Medicine* (Ed.: M. Baranska), Springer Netherlands, Dordrecht, **2014**, pp. 329–354.
[59] B. G. Frushour, J. L. Koenig, *Biopolymers* **1974**, *13*, 1809.

[60] S. N. Kalkura, V. Ramakrishnan, S. Devanarayanan, *Infrared Phys.* **1987**, *27*, 335.
[61] N. C. Maiti, M. M. Apetri, M. G. Zagorski, P. R. Carey, V. E. Anderson, *J. Am. Chem. Soc.* **2004**, *126*, 2399.
[62] T. Kitagawa, Y. Kygogoku, T. Iizuka, M. Ikeda-Saito, T. Yamanaka, *J. Biochem.* **1975**, *78*, 719.
[63] R. Tuma, *J. Raman Spectrosc.* **2005**, *36*, 307.
[64] C. D. Syme, E. W. Blanch, C. Holt, R. Jakes, M. Goedert, L. Hecht, L. D. Barron, *Eur. J. Biochem.* **2002**, *269*, 148.
[65] M. S. Bergholt, W. Zheng, K. Lin, K. Y. Ho, M. Teh, K. G. Yeoh, J. B. Y. So, Z. Huang, *J. Biomed. Opt.* **2011**, *16*, 037003.
[66] K. De Gussem, P. Vandenabeele, A. Verbeken, L. Moens, *Spectrochim. Acta A Mol. Biomol. Spectrosc.* **2005**, *61*, 2896.
[67] I. Pence, A. Mahadevan-Jansen, *Chem. Soc. Rev.* **2016**, *45*, 1958.
[68] M. J. Benecky, R. A. Copeland, R. P. Rava, R. Feldhaus, R. D. Scott, C. M. Metzler, D. E. Metzler, T. G. Spiro, *J. Biol. Chem.* **1985**, *260*, 11671.
[69] S. Nagatomo, M. Nagai, N. Shibayama, T. Kitagawa, *Biochemistry* **2002**, *41*, 10010.
[70] C. Wang, U. Neugebauer, J. Bürck, M. Myllykoski, P. Baumgärtel, J. Popp, P. Kursula, *PLoS One* **2011**, *6*, e19915.
[71] N. C. Shah, O. Lyandres, J. T. Walsh, M. R. Glucksberg, R. P. Van Duyne, *Anal. Chem.* **2007**, *79*, 6927.
[72] M. Pézolet, M. Pigeon, D. Ménard, J. P. Caillé, *Biophys. J.* **1988**, *53*, 319.
[73] A. Rygula, K. Majzner, K. M. Marzec, A. Kaczor, M. Pilarczyk, M. Baranska, *J. Raman Spectrosc.* **2013**, *44*, 1061.
[74] G. J. Thomas Jr, B. Prescott, M. G. Hamilton, *Biochemistry* **1980**, *19*, 3604.
[75] D. Kurouski, R. P. Van Duyne, I. K. Lednev, *Analyst* **2015**, *140*, 4967.
[76] C. M. Cowan, S. Quraishe, S. Hands, M. Sealey, S. Mahajan, D. W. Allan, A. Mudher, *Sci. Rep.* **2015**, *5*, 17191.
[77] R. Buividas, N. Dzingelevičius, R. Kubiliūtė, P. R. Stoddart, V. Khanh Truong, E. P. Ivanova, S. Juodkazis, *J. Biophotonics* **2015**, *8*, 567.

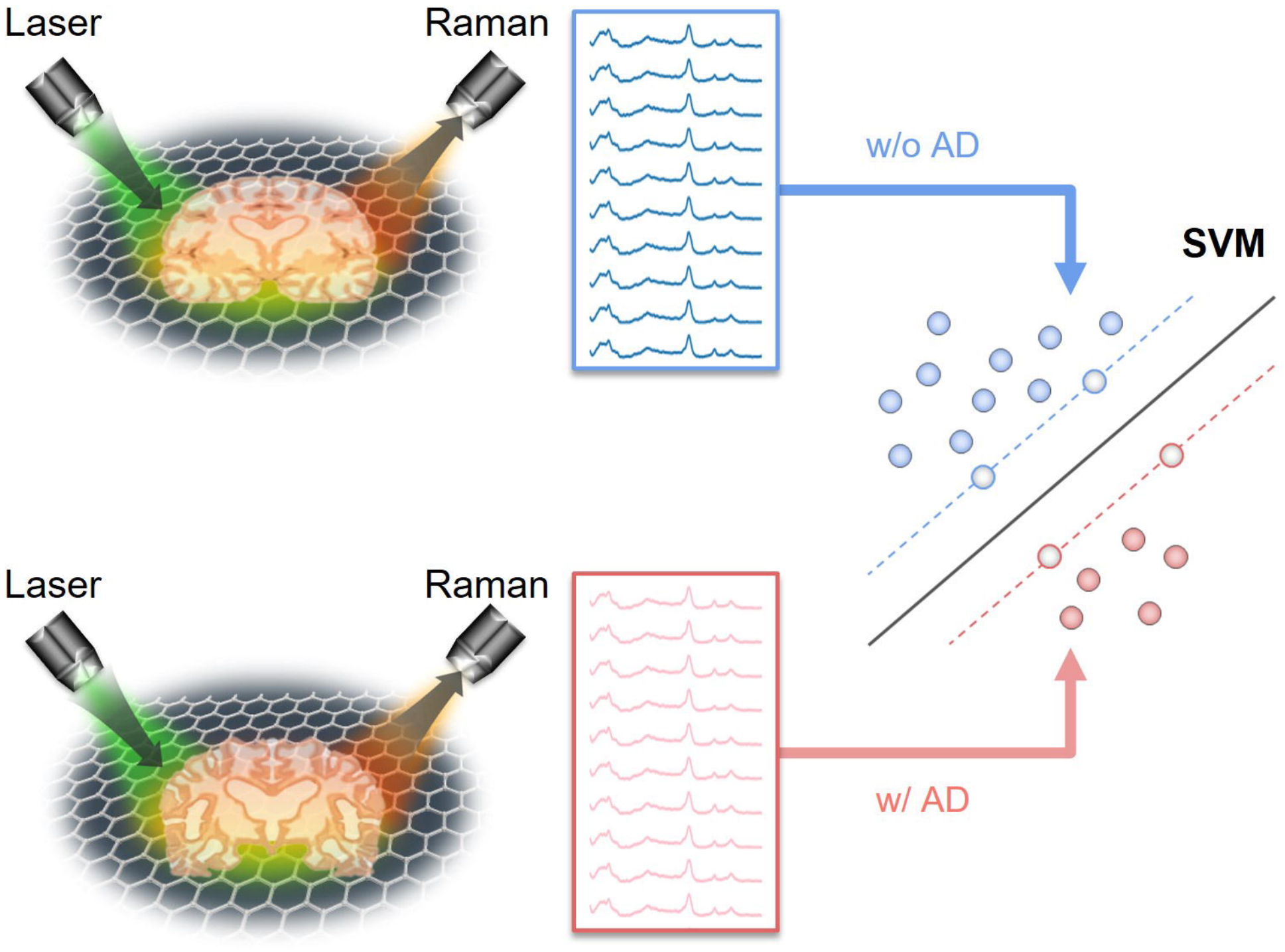
Laser
Raman
w/o AD
SVM
Laser
Raman
w/ AD

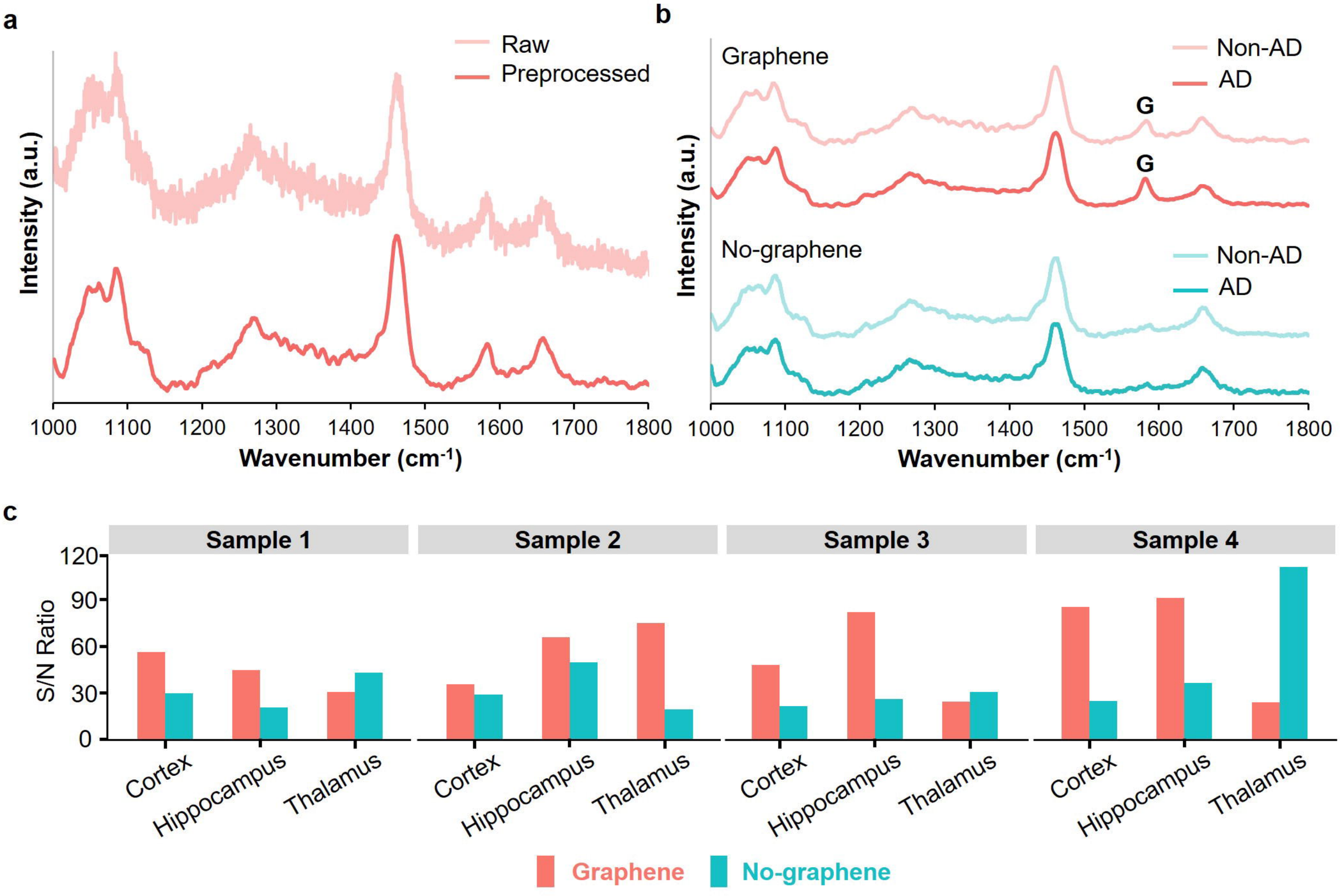
a
Raw
Preprocessed
Intensity (a.u.)
1000
1100
1200
1300
1400
1500
1600
1700
1800
Wavenumber (cm-1)
b
Graphene
Non-AD
AD
G
G
No-graphene
Non-AD
AD
Intensity (a.u.)
1000
1100
1200
1300
1400
1500
1600
1700
1800
Wavenumber (cm-1)
c
Sample 1
Sample 2
Sample 3
Sample 4
S/N Ratio
120
90
60
30
0
Cortex
Hippocampus
Thalamus
Graphene
No-graphene

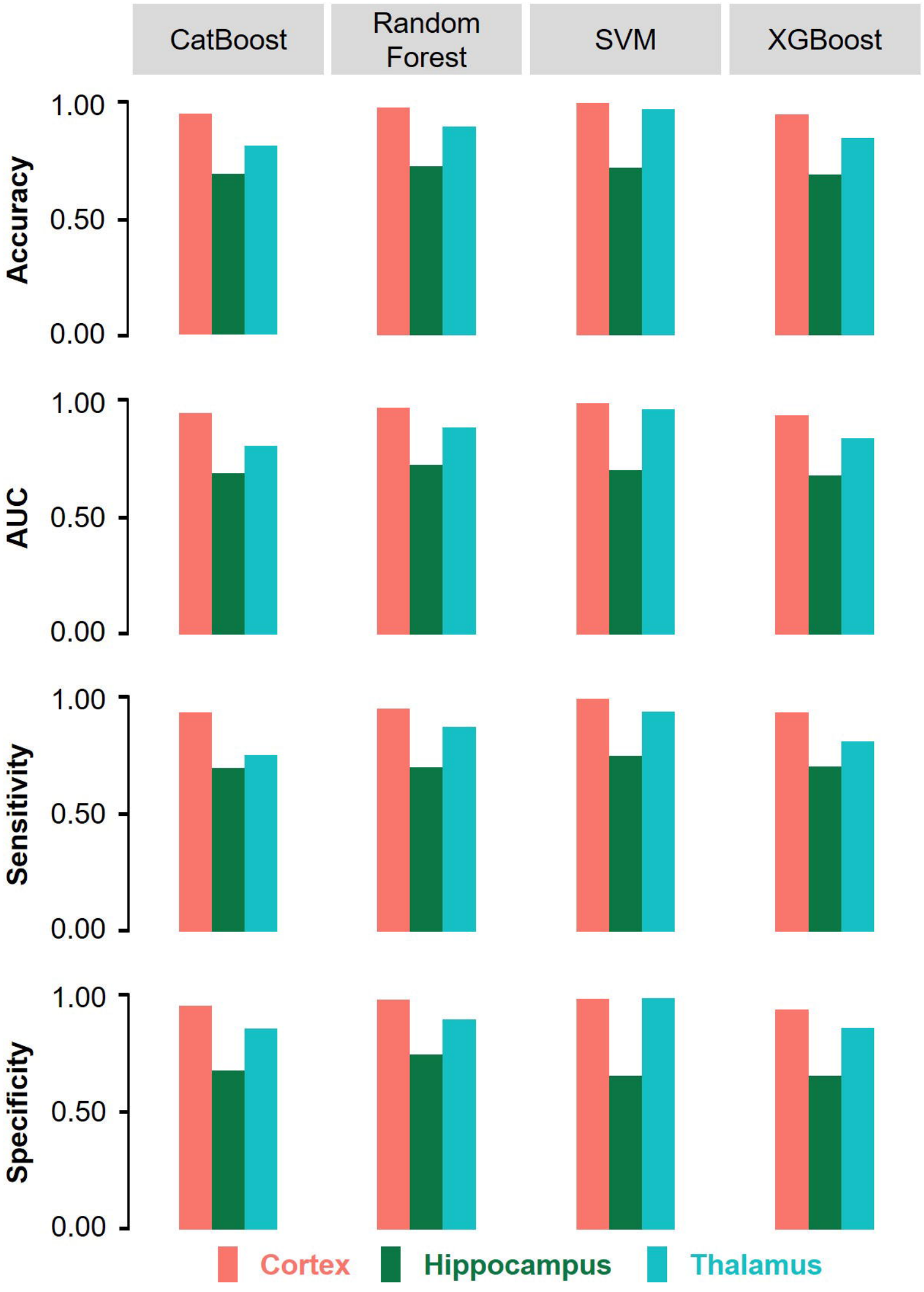
CatBoost
Random Forest
SVM
XGBoost
Accuracy
AUC
Sensitivity
Specificity
1.00
0.50
0.00
Cortex
Hippocampus
Thalamus

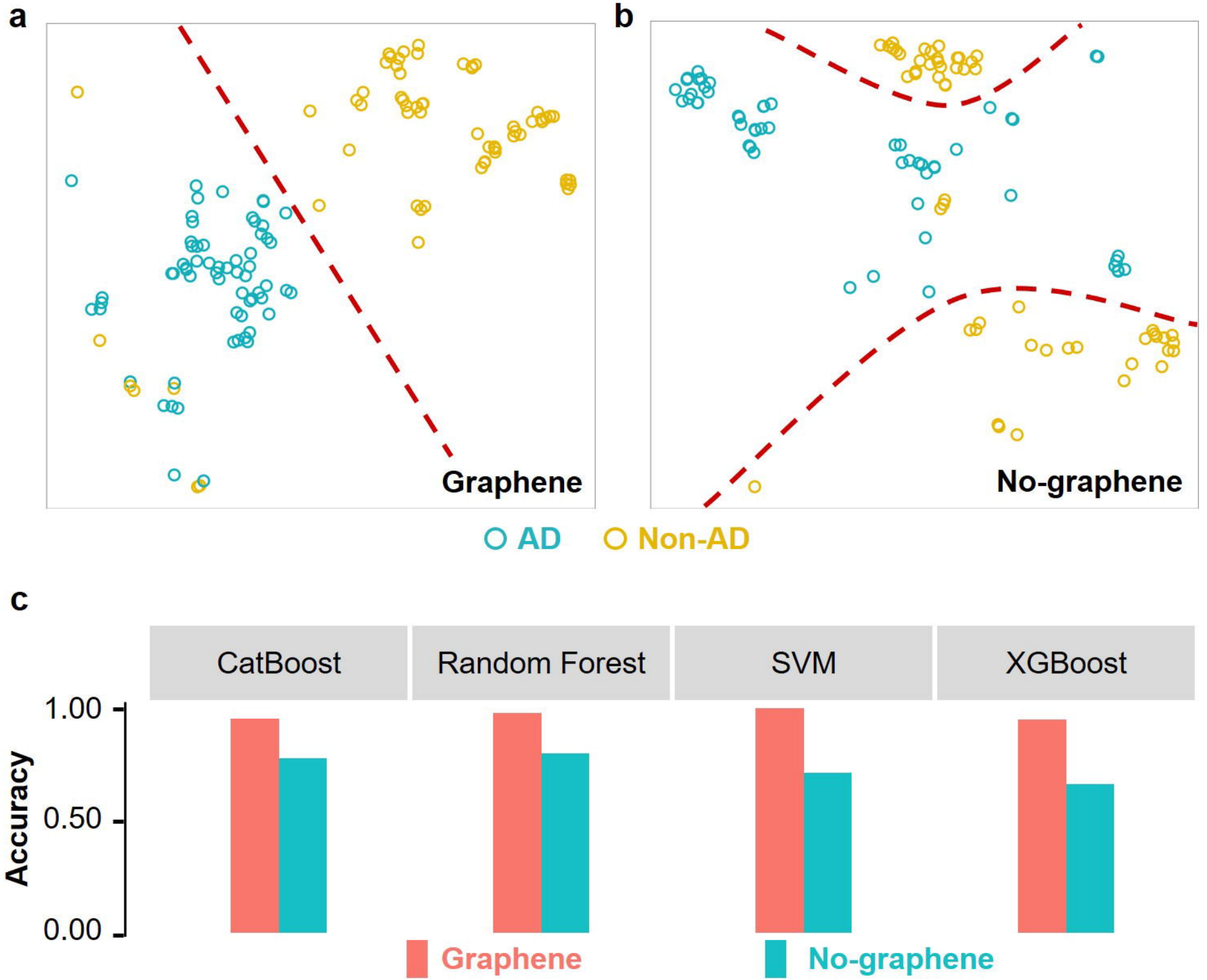
a
Graphene
b
No-graphene
AD
Non-AD
c
CatBoost
Random Forest
SVM
XGBoost
Accuracy
1.00
0.50
0.00
Graphene
No-graphene

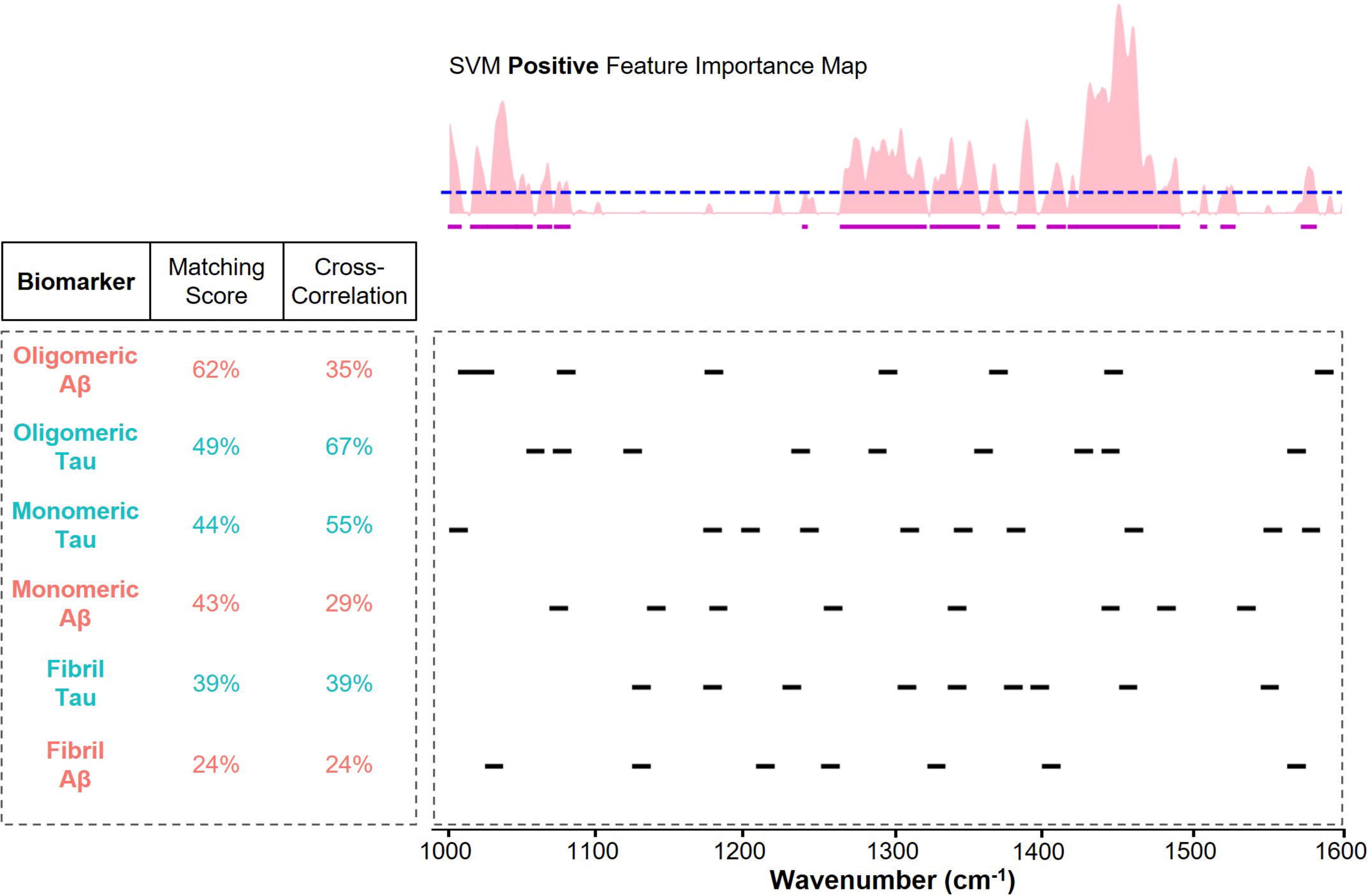
SVM **Positive** Feature Importance Map
Biomarker
Matching Score
Cross-Correlation
Oligomeric Aβ
62%
35%
Oligomeric Tau
49%
67%
Monomeric Tau
44%
55%
Monomeric Aβ
43%
29%
Fibril Tau
39%
39%
Fibril Aβ
24%
24%
1000
1100
1200
1300
1400
1500
1600
Wavenumber (cm-1)

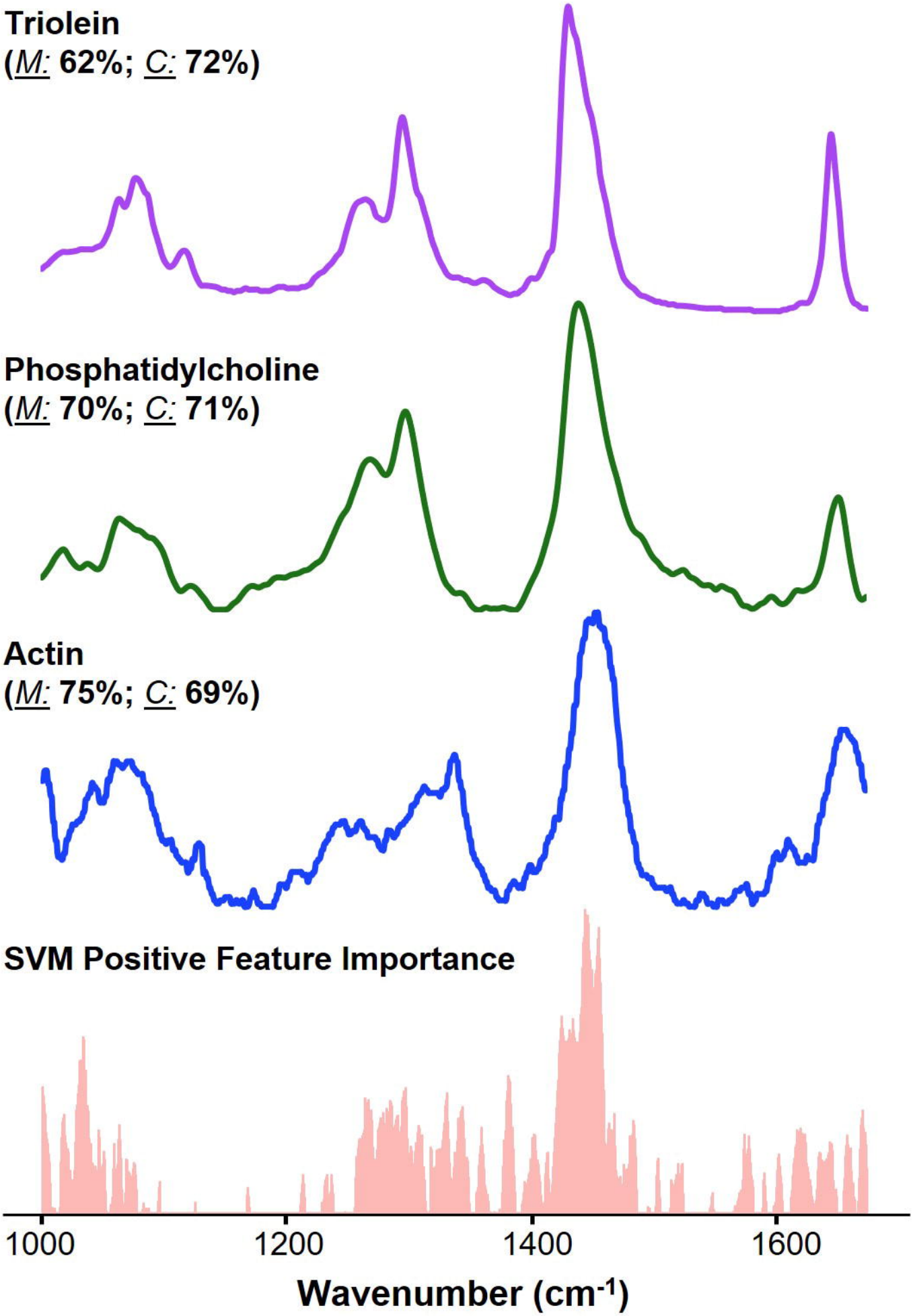
Triolein
(M: 62%; C: 72%)
Phosphatidylcholine
(M: 70%; C: 71%)
Actin
(M: 75%; C: 69%)
SVM Positive Feature Importance
1000
1200
1400
1600
Wavenumber (cm-1)

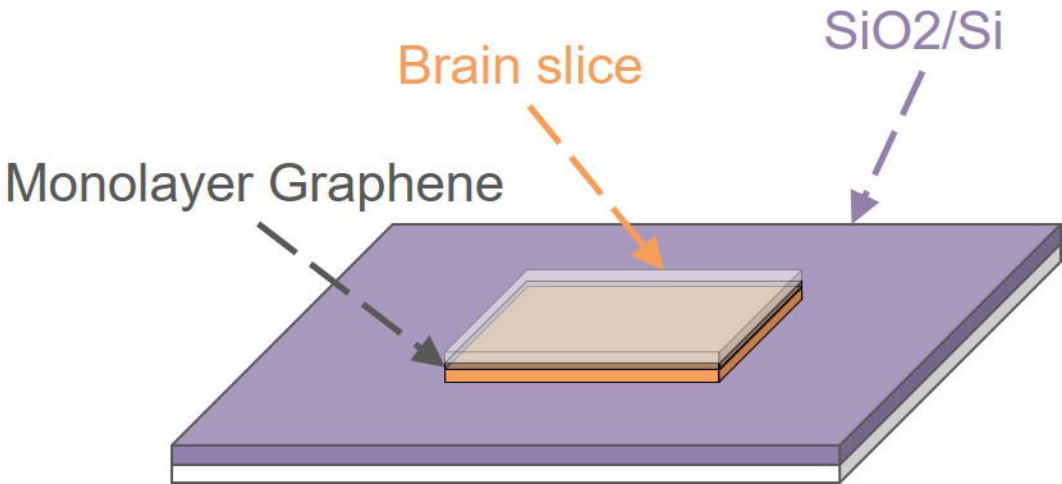
SiO2/Si
Brain slice
Monolayer Graphene

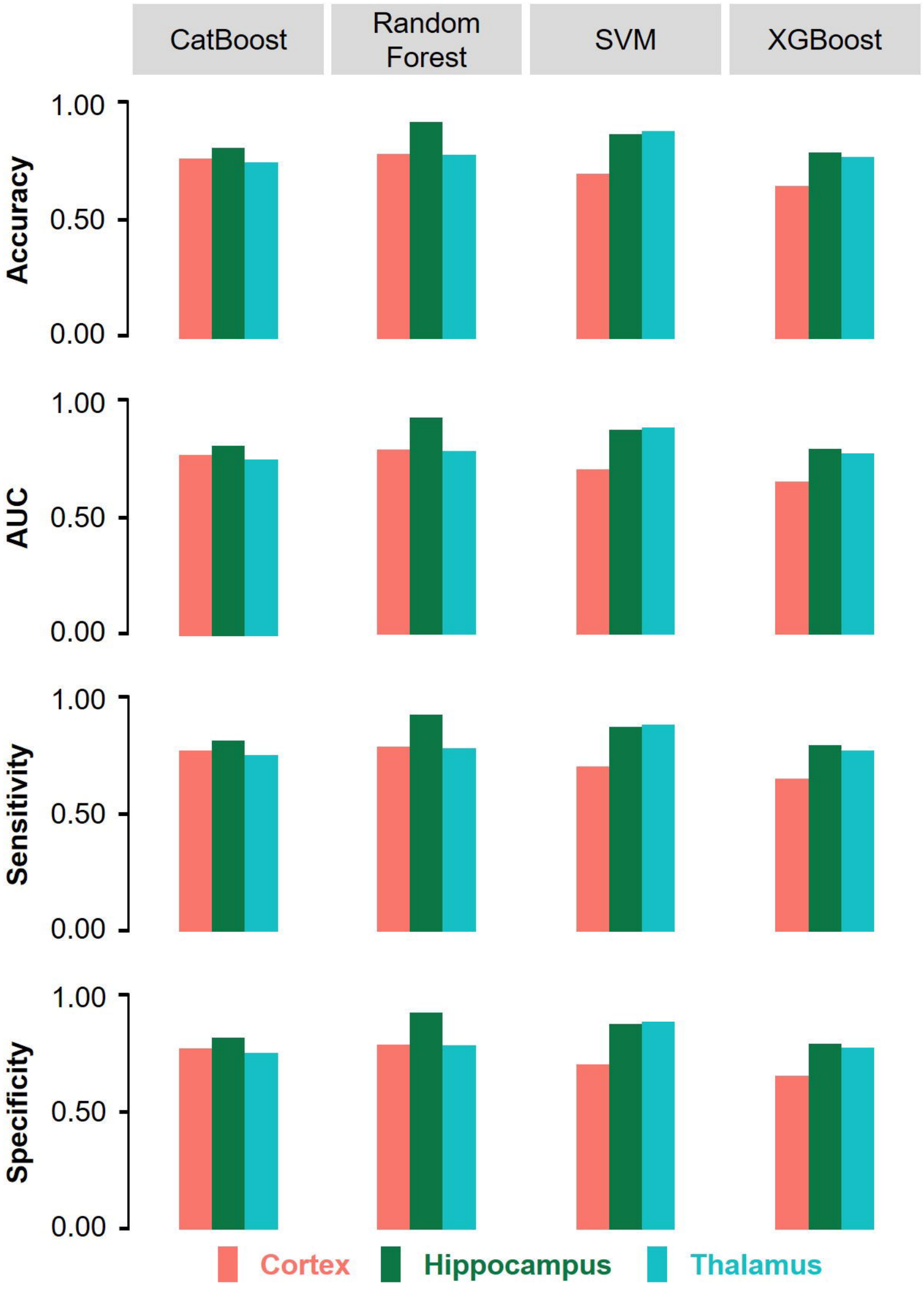
CatBoost
Random Forest
SVM
XGBoost
Accuracy
AUC
Sensitivity
Specificity
1.00
0.50
0.00
Cortex
Hippocampus
Thalamus

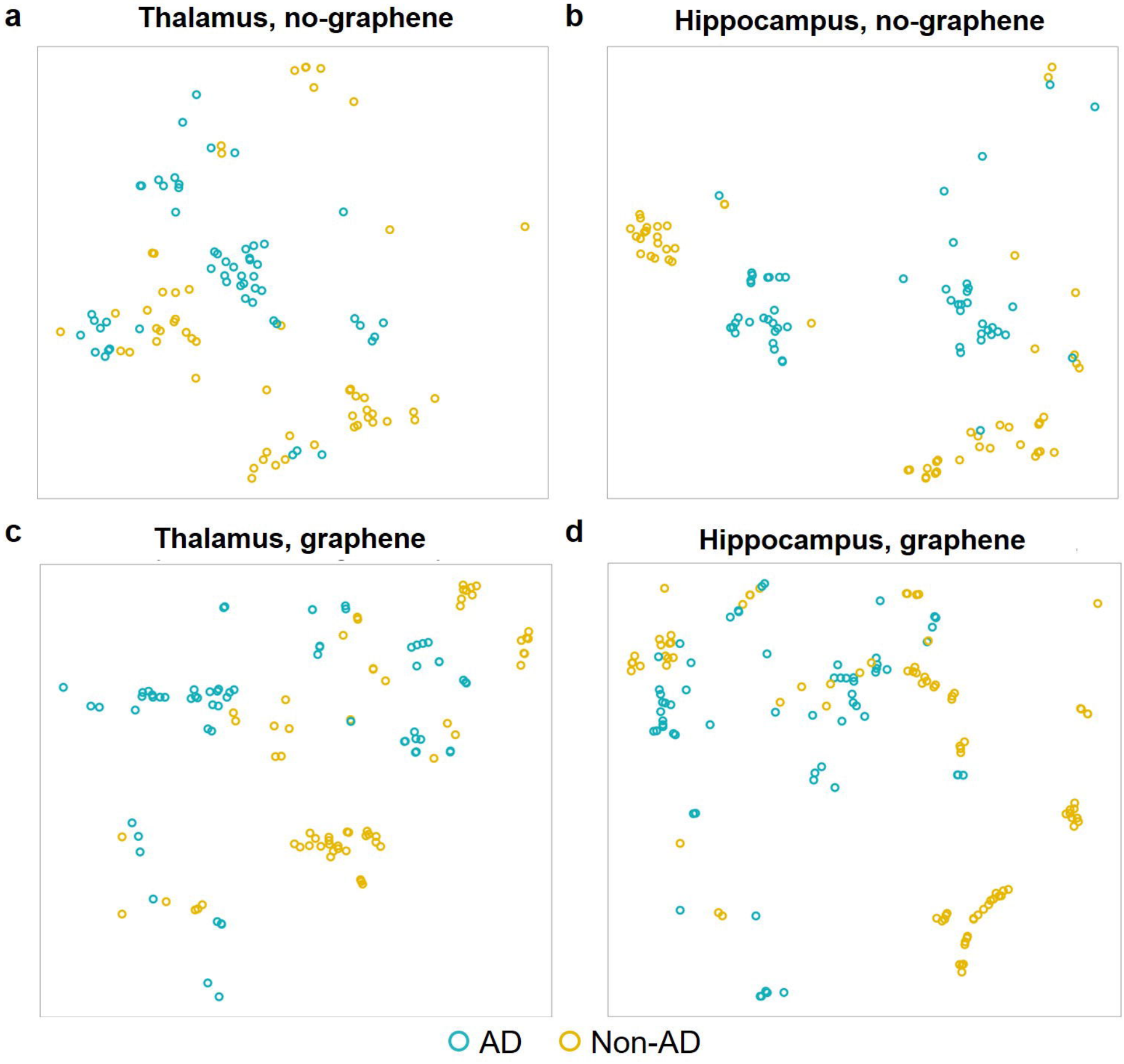
a
Thalamus, no-graphene
b
Hippocampus, no-graphene
c
Thalamus, graphene
d
Hippocampus, graphene
AD
Non-AD

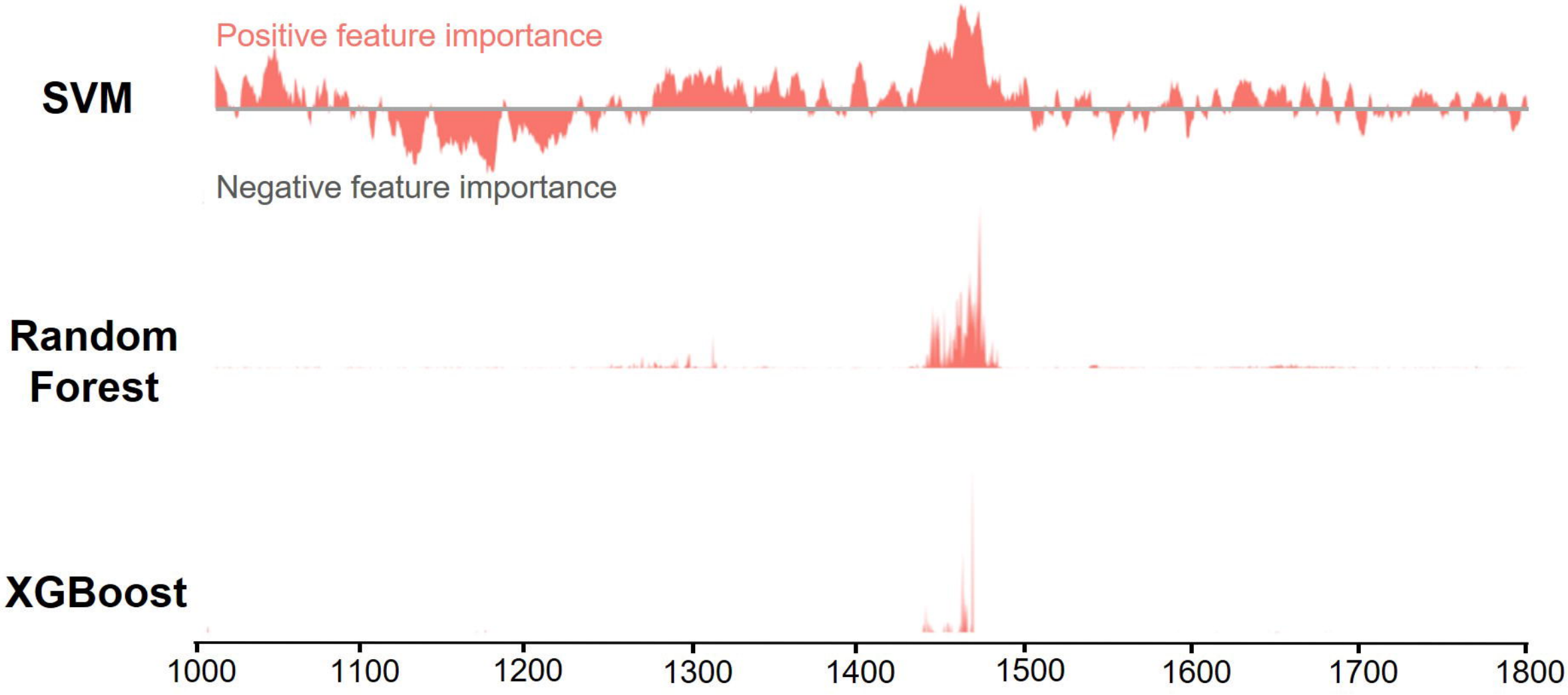
Positive feature importance
SVM
Negative feature importance
Random Forest
XGBoost
1000
1100
1200
1300
1400
1500
1600
1700
1800